Applied Catalysis B: Environmental 297 (2021) 120500

Contents lists available at ScienceDirect

Applied Catalysis B: Environmental

journal homepage: www.elsevier.com/locate/apcatb

The enhanced near-infrared photocatalytic and photothermal effects of MXene-based heterojunction for rapid bacteria-killing

Qian Wu [a], Lei Tan [a], Xiangmei Liu [a,*], Zhaoyang Li [b], Yu Zhang [c,**], Yufeng Zheng [c,d,**], Yanqin Liang [b], Zhenduo Cui [b], Shengli Zhu [b], Shuilin Wu [a,b,*]

[a] Biomedical Materials Engineering Research Center, Collaborative Innovation Center for Advanced Organic Chemical Materials Co-constructed by the Province and Ministry, Hubei Key Laboratory of Polymer Materials, Ministry-of-Education Key Laboratory for the Green Preparation and Application of Functional Materials, School of Materials Science & Engineering, Hubei University, Wuhan, 430062, China

[b] School of Materials Science & Engineering, The Key Laboratory of Advanced Ceramics and Machining Technology by the Ministry of Education of China, Tianjin University, Tianjin, 300072, China

[c] Department of Orthopedics, Guangdong Provincial People's Hospital, Guangdong Academy of Medical Sciences, Guangzhou, 50080, China

[d] State Key Laboratory for Turbulence and Complex System and Department of Materials Science and Engineering, College of Engineering, Peking University, Beijing, 0087, China

ARTICLE INFO

Keywords:
MXene
Heterojunctions
Photothermal
Photocatalytic
Antibacterial

ABSTRACT

Bacterial resistance threatens the health of human beings when they combat pathogenic diseases with antibiotics. Herein, an ecofriendly and antibiotics-free 0D/2D Schottky heterojunction (Ag_2S/Ti_3C_2) was synthesized for the first time to treat bacterial infection with a high efficacy of 99.99% within 20 min under 808 nm NIR light irradiation, which was ascribed to the synergy of enhanced photocatalytic and photothermal effects. The density functional theory calculations show that when a redistribution of charge occurs at the interface between Ag_2S and Ti_3C_2 due to the difference in their Fermi energy levels (E_F), it results in an upward bend of the Ag_2S energy band. Additionally, in the case of Ag_2S/Ti_3C_2, the higher conduction band energy of Ag_2S compared to the E_F of Ti_3C_2 and the excellent electrical conductivity of the latter made the photoexcited electrons in Ag_2S, including those hot electrons produced by surface plasma resonance (SPR), rapidly flow to Ti_3C_2, thus greatly increasing both photocatalytic and photothermal performance of Ti_3C_2. *In vitro* and *in vivo* tests showed that this photoresponsive system possessed not only highly effective antibacterial efficacy against *Staphylococcus aureus* infection but also excellent biocompatibility simultaneously. Therefore, this hybrid is expected to be a promising ecofriendly platform for the rapid treatment of bacterial infections using NIR light.

1. Introduction

A range of diseases caused by bacterial infections poses serious threats to human health. Each year, approximately 17 million people worldwide die from infectious diseases caused by pathogenic bacteria, and this number is increasing rapidly [1]. Among them, *Staphylococcus aureus* (*S. aureus*) is one of the most common pathogenic bacteria, with roughly 30% of the population colonized by this microorganism [2], which has caused a variety of human diseases such as meningitis, osteomyelitis [3], wound infections, and pneumonia. For a long time, the discovery of antibiotics largely alleviated the adverse effects caused by bacterial infections [4].

However, the misuse of antibiotics has contributed to the rapid development and spread of bacterial resistance to antibiotics. The emergence of bacterial drug resistance has made once-treatable diseases deadly again, which has been greatly undermining the achievements of modern medicine [5]. Although a new generation of antibiotics can be effective in killing existing drug-resistant bacteria, developing new antibiotics is not only expensive but also time-consuming. In contrast, it takes only a few weeks for bacteria to develop antibiotic resistance. As a

* Corresponding author at: Biomedical Materials Engineering Research Center, Collaborative Innovation Center for Advanced Organic Chemical Materials Co-constructed by the Province and Ministry, Hubei Key Laboratory of Polymer Materials, Ministry-of-Education Key Laboratory for the Green Preparation and Application of Functional Materials, School of Materials Science & Engineering, Hubei University, Wuhan, 430062, China.

** Corresponding author at: Department of Orthopedics, Guangdong Provincial People's Hospital, Guangdong Academy of Medical Sciences, Guangzhou, 50080, China.

E-mail addresses: liuxiangmei978@63.com (X. Liu), luck_200@26.com (Y. Zhang), yfzheng@pku.edu.cn (Y. Zheng), shuilinwu@tju.edu.cn (S. Wu).

https://doi.org/10.1016/j.apcatb.2021.120500
Received 11 April 2021; Received in revised form 17 June 2021; Accepted 27 June 2021
Available online 29 June 2021

result, the rate of development of new antibiotics has not kept pace with the rising rate of bacterial resistance [6]. For this reason, there is an urgent need to develop safe and rapid therapeutic strategies as an effective alternative to conventional antibiotics for the treatment of bacterial infections without inducing bacterial resistance.

Currently, many antibiotic-free strategies have been employed to treat bacterial infections through various methods, such as releasing metallic ions [7], electrostatic adsorption, releasing radical oxygen species (ROS) [8], locally increasing temperature [9], and puncturing bacterial membranes by keen-edged nanoneedles [10]. Among them, near-infrared (NIR) light-based phototherapy, including photothermal therapy (PTT) and photodynamic therapy (PDT), is one of the most promising therapeutic strategies due to its deep penetration, biosafety, and rapid and highly effective therapeutic efficacy without bacterial resistance [11,12].

PTT is based on the rapid increase of local temperature, which will denature and inactivate the proteins in the bacteria and lead to bacterial death [13]. PDT is a treatment that excites photosensitizers by light to produce ROS, which can cause severe oxidative damage to bacteria and their final death [14]. Studies have shown that treatment of bacterial infections *in vivo* by applying safe photoinduced heat (less than 55 °C) will not cause damage to healthy tissue [15]. In addition, the local heat generated by the photothermal effect increases the permeability of the bacterial cell membrane, making it easier for antibacterial substances such as reactive oxygen species (ROS) from the environment to enter the bacteria and thus inactivate them. Therefore, a synergistic antibacterial strategy using PTT-enhanced PDT can achieve the effective eradication of bacteria at lower temperatures [16].

Besides its photothermal, excellent biocompatibility and chemical stability, the narrow band gap of 0.9 eV allows Ag_2S to be excited by NIR light for photocatalytic reactions [17–20]; hence, this material has been used for phototherapy [21]. However, the narrow band gap can accelerate the recombination of photogenerated electrons and holes in Ag_2S, thus greatly limiting its photocatalytic reaction [22]. Recently, MXene, a new type of two-dimensional material [23], has attracted much attention and been applied in a variety of fields such as water treatment, catalysis [24,25], intracellular fluorescence imaging, antibacterial [26], and anticancer treatment, due to its unique structure and ideally tunable physicochemical properties together with its good biocompatibility and NIR-responsive properties [27].

Furthermore, the ultra-high electron conductivity of MXene makes it easy for electrons to flow from the semiconductors to its surface, thus ensuring effective electron-hole separation. At the same time, the high specific surface area of MXene provides more reactive sites for photocatalytic reactions [28]. In addition, the abundant hydrophilic groups on the surface of MXene enable it not only to easily establish strong links with various semiconductors, but also to interact strongly with water molecules, which ensures the stable performance of MXene in aqueous solutions [29]. In view of the aforementioned, we propose a hypothesis concerning if a Schottky heterojunction of Ag_2S/Ti_3C_2 can be constructed with enhanced photocatalytic and photothermal performance through a continuous flow of NIR-excited electrons including those hot electrons produced by local surface plasma resonance (LSPR) from Ag_2S to Ti_3C_2 at the interface between them.

In this work, based on the above hypothesis, a novel 0D/2D Schottky heterojunction of Ag_2S/Ti_3C_2 was prepared for the treatment of bacteria-infected wounds by the synergy of PTT and PDT under NIR light irradiation. Ag_2S nanoparticles were grown *in situ* on the surface of two-dimensional Ti_3C_2 using a simple wet chemical method. The structure and photocatalytic mechanism of Ag_2S/Ti_3C_2 heterojunction were investigated in detail by DFT calculations. Subsequent *in vitro* and *in vivo* results showed that the introduction of Ti_3C_2 greatly enhanced the photocatalytic and photothermal performance of Ag_2S, which endowed the hybrid with highly effective antibacterial efficacy under NIR light irradiation within a short time.

2. Experimental section

2.1. Preparation of samples

2.1.1. Pretreatment of MXene

At room temperature, Ti_3AlC_2 (purchased from Nanjing Mingshan New Material Co., Ltd., 99.5%) was dispersed in HF solution to etch Al to prepare Ti_3C_2. Generally, 5 g of Ti_3AlC_2 powder was dispersed in 50 mL of HF aqueous solution (40%) and soaked at room temperature for 24 h. After the etching process was completed, the sample was collected by centrifugation and washed with deionized water and ethanol to obtain Ti_3C_2.

The Ti_3C_2 etched by the HF was dispersed in 50 mL DMSO and magnetically stirred at room temperature for 36 h. After the intercalation process was completed, the sample was collected by centrifugation and washed with deionized water and ethanol, and then the powder was freeze-dried and collected.

2.1.2. Preparation of Ti_3C_2 nanosheets

The intercalated Ti_3C_2 powder was sonicated for layer exfoliation. Generally, 0.5 g of Ti_3C_2 black powder was dispersed in 75 mL of deionized water and sonicated with a high-powered ultrasonic cleaner for 4.5 h. The samples were then collected by centrifugation and washed repeatedly with deionized water and ethanol to obtain pure Ti_3C_2 nanosheets.

2.1.3. Synthesis of Ag_2S/Ti_3C_2 hybrids

10 mL of aqueous solution containing 0.15 g of thiourea (Tu) was prepared, to which 11 drops of ammonia at a concentration of 7% were added. Ti_3C_2 nanosheets were weighed according to the different mass ratios (10%, 20%, and 40%) of Ti_3C_2 nanosheets to Ag_2S, and then dissolved in 10 mL of deionized water and dispersed homogeneously by sonication. We then added 10 mL of uniform Ti_3C_2 dispersion into the TU solution and stirred it magnetically for 15 min. At the same time, 10 mL 0.3 M $AgNO_3$ aqueous solution was prepared. A 10 mL $AgNO_3$ aqueous solution was slowly added drop by drop to the above mixed solution to initiate the reaction, and magnetic stirring was conducted at room temperature for 30 min. After the reaction was completed, the complex products were collected by centrifugation (12,000 rpm/min, 10 min), then alternately washed with deionized water and ethanol three times, and finally dried in a vacuum at 60 °C.

2.1.4. Synthesis of pure Ag_2S nanoparticles

10 mL of deionized water was used to replace 10 mL of homogeneous Ti_3C_2 dispersion in the above reaction, and the rest of the synthesis process was kept constant. The successful synthesis of Ag_2S nanoparticles was indicated when the color of the solution changed from colorless to deep black within 30 min after initiating the reaction.

2.2. Characterization

The crystal structure of the samples was measured by X-ray diffraction (XRD, D8A25, Bruker, Germany). The Raman spectra of the materials were measured by inVia Reflex Raman microspectrometer (Renishaw, England). X-ray photoelectron spectroscopy (XPS) was obtained with an instrument (ESCALAB 250 XI, Thermo Scientific, USA). *In situ* and *ex situ* XPS measurements of the materials were detected by X-ray photoelectron spectrometer (ThermoFischer, ESCALAB 250Xi). The nitrogen adsorption and desorption behaviors of materials at 77 K were determined by Brunauer-Emmett-Teller (BET, JW-BK112). The microscopic morphology, structure and crystal structure of the samples were observed with field emission scanning electron microscopy (FE-SEM, ZEISS Sigma 500, Germany) equipped with energy-dispersive spectroscopy (EDS) and a high-resolution transmission electron microscope (HRTEM, Titan G260−300). The absorption spectra of the aqueous solutions of the materials and the absorbance at 808 nm were determined

by the enzyme calibrator (SpectraMax i3) (Molecular Devices). The diffuse reflectance spectrum of the material was obtained by UV-3600 ultraviolet–visible–near infrared (UV–vis-NIR) spectrophotometer (Shimadzu, Japan) measurement. The model number of the instrument used to measure ultraviolet photoelectron spectroscopy (UPS) is PHI5000 VersaProbe III (Scanning ESCA Microprobe) SCA (Spherical Analyzer). During the test, the sample bias was −5 V. The photoluminescence (PL) emission spectra of the materials were obtained by fluorescence spectrophotometer (LS-55, Perkin Elmer, USA) measurements.

2.3. Theoretical calculation details

In our calculation process, all the spin theoretical simulations were carried out on the Vienna Ab-initio Simulation Package (VASP), version 5.4.1 [30]. Generalized gradient approximation (GGA) in the form of Perdew-Burke-Emzerhof (PBE) [31] function was used to evaluate electron-electron exchanges and related interactions, and a projector enhanced wave (PAW) method was implanted to represent the nuclear-electron (valence electron) interactions effect. The plane-wave basis function set a dynamic cut-off energy of 500 eV. A Monkhorst-Pack meshes [32] with a size of 5 × 5 × 5 was used to sample the bulk Brillouin zone, and 5 × 5 × 1 was for the surface. The geometry of the ground-state atoms was optimized by reducing the force below 0.02 eV/Å and setting the convergence criterion for energy to 1.0×10^{-5} eV/cell. The accuracy of the electronic structure and total energy calculation results was ensured by using the Gaussian method. Van der Waal (vdw) interactions were included in Grimme's DFT-D3 method [33] described to obtain a better description of intermolecular interactions.

2.4. Photocatalytic properties testing of materials

2.4.1. Photoelectrochemical detection

The sample was configured into a homogeneous aqueous dispersion with a concentration of 5 mg/mL, and subsequently 50 μL of the material solution was added dropwise onto the surface of a 6 mm diameter titanium sheet. After the sample on the surface of the titanium sheet was completely dried, it was used as the working electrode. The reference electrode was the Ag/AgCl electrode and the platinum electrode was the counter electrode. The photoelectrochemical properties of the samples in Na_2SO_4 (0.5 M) electrolyte were measured in a standard three-electrode system using an electrochemical workstation (PGSTAT302N, AUT87820, Netherlands) under 808 nm laser irradiation conditions.

2.4.2. Detection of photocatalytic generation of reactive oxygen species

2,7-Dichlorofluorescein diacetate (DCFH-DA) was used as a reactive oxygen fluorescent probe to detect the total amount of reactive oxygen species produced by the samples under irradiation. Briefly, 180 μL of DCFH was taken in a 96-well plate, followed by the addition of 20 μL of aqueous material solution (5 mg/mL) and mixed well. For the Ctrl group, 20 μL of deionized water was added. Each well was irradiated with an 808 nm laser for 20 min, and the fluorescence intensity of the solution (excitation wavelength 488 nm and absorption wavelengths 525 nm) was recorded every two minutes using an enzyme marker.

The production of $^1O_2$ during photocatalysis was detected using 1,3-Diphenylisobenzofuran (DPBF). We added 180 μL of DPBF DMSO solution (10 μg/mL) to the 96-well plate, followed by 20 μL of material aqueous solution (5 mg/mL). All samples were shaken for 10 min under dark conditions to mix well. After irradiation at 808 nm NIR for 20 min, the absorption spectra of the solutions were detected by enzyme standardization.

The electron spin resonance (ESR) spectra of the materials were measured by a JES-FA200 spectrometer (JEOL, Tokyo, Japan). Briefly, $^1O_2$ production during Ag_2S/Ti_3C_2-20 photocatalysis was measured by electron spin resonance under 808 nm NIR laser irradiation conditions with 2,2,6,6-tetramethylpiperidine (Aladdin) as a spin trap.

2.5. Photothermal performance testing of materials

2.5.1. Photothermal heating curve and heating thermal image

200 μL of aqueous solution of the material at a concentration of 500 μg/mL was taken in a 96-well plate and irradiated with an 808 NIR laser (0.67 W/cm^2). The temperature of the samples was recorded and photographed every 60 s with a FLIR thermal camera (FLIR-E50, Estonia).

2.5.2. Photothermal cycle curve

Like the above procedure, the temperature of Ag_2S/Ti_3C_2-20 was recorded every minute under the condition that the 808 NIR laser was turned on for 20 min followed by 20 min off for a photothermal cycle. This process was repeated five times.

2.5.3. Photothermal conversion efficiency calculation

The Ag_2S/Ti_3C_2-20 photothermal conversion efficiency (η) is obtained by the following equation (Eq. (2.1)) [34]:

$$\eta = \frac{hS(T_{max} - T_0) - Q}{I(1 - 10^{-A})}, \tag{2.1}$$

where h is the heat transfer coefficient, S is the surface area of the vessel, T_{max} is the maximum equilibrium temperature during heating, T_0 indicates the ambient temperature, Q is the heat absorption rate of the 96-well plate (polystyrene), I represents the 808 NIR laser power, and A is the absorbance of Ag_2S/Ti_3C_2-20 at 808 nm.

The time constant (τ_S) for Ag_2S/Ti_3C_2-20 was calculated by equation (Eq. (2.2)) during the cooling process.

$$t = -\tau_S \ln\theta = -\tau_S \ln\frac{T - T_0}{T_{max} - T_0} \tag{2.2}$$

At this point, assuming that the thermal input and output of the system are equal,

the

$$hS = \frac{\sum_i m_i C_{p,i}}{\tau_S} \approx \frac{m_{H_2O}\ C_{H_2O}}{\tau_S} \tag{2.3}$$

In formula (Eq. (2.3)), m_{H_2O} and C_{H_2O} are the mass of water and the specific heat capacity of water, respectively.

2.6. In vitro antimicrobial test

The *in vitro* antimicrobial properties of the materials were quantitatively evaluated with bacterial plate coating under photoexcitation. *S. aureus* was cultured in a standard Luria-Bertani (LB) culture medium. A density of 5×10^6 CFU/mL of *S. aureus* solution was added to the 96-well plate with 180 μL, followed by 20 μL of material solutions (Ti_3C_2, Ag_2S, Ag_2S/Ti_3C_2-10, Ag_2S/Ti_3C_2-20, and Ag_2S/Ti_3C_2-40) at a concentration of 5 mg/mL to the experimental group and 20 μL to the Ctrl with sterilized PBS. Each well was irradiated with an 808 nm laser (0.67 W/cm^2) for 20 min, during which the temperature was kept at about 55 °C to avoid the effect of high temperature. In the dark group, the material was co-cultured with the bacteria for 20 min under dark conditions. After the completion of the antibacterial treatment, the bacterial solution in the wells was blown evenly and diluted, and the bacterial plate-coating operation was performed on standard LB agar. This was followed by incubation at 37 °C for 24 h. The calculation of antimicrobial rates was performed according to the following equation (Eq. (2.4)):

$$\text{Antibacterial ratio}\ (\%) = \frac{\mathrm{C} - \mathrm{S}}{\mathrm{C}} \times 100\% \tag{2.4}$$

where C and S stand for the numbers of bacteria (CFUs) in the control and sample groups, respectively.

The experimental procedures for the research on the antibacterial properties of materials against *Escherichia coli* (*E. coli*) are consistent with the above-mentioned antibacterial experimental procedures.

2.7. Antibacterial mechanism testing

2.7.1. Live/dead fluorescent staining of bacteria

After completion of the *in vitro* light/dark antimicrobial operation as described above, the bacterial solution in 96-well plate was discarded and 100 μL of live/dead fluorescent dye (SYTO9 and PI, LIVE/DEAD Baclight Bacterial Viability Kit, Beyotime) was added in. Subsequently, the well plate was incubated at 37 °C for 20 min. We discarded the dye from the well plate and washed gently with sterilized PBS 3 times. The well plate was dried away from light and photographed with an inverted fluorescence microscope (Olympus, IX73, Japan); live bacteria fluoresce in green while dead bacteria fluoresce in red.

2.7.2. Bacterial morphology observation

After completion of the antimicrobial test, the bacterial solution in the well plate was discarded and washed three times with sterilized PBS. Subsequently, 200 μL of 2.5% glutaraldehyde solution was added to each well for 2 h to fix the bacteria. The wells were washed three times with sterilized PBS and then each well was dehydrated by adding 200 μL of different concentrations of ethanol in a gradient (30%, 50%, 70%, 90%, and 100%) for 15 min each time. After the samples were dried, the bacterial morphology was observed by FE-SEM and photographed.

2.8. Statistical analysis

All the quantitative data were evaluated and analyzed as mean values ± standard deviations and contrasted *via* one-way analysis of variance (ANOVA). Values of $^{*}P < 0.05$, $^{**}P < 0.01$, $^{***}P < 0.001$, and $^{****}P < 0.0001$ were considered statistically significant.

3. Results and discussion

3.1. Characterization of synthesized Ag_2S/Ti_3C_2 hybrids

3.1.1. Synthesis of heterojunction

The preparation process of Ag_2S/Ti_3C_2 hybrids is schematically shown in Fig. S1, illustrating that Ag_2S nanoparticles [35] are uniformly distributed on the surface of Ti_3C_2 nanosheets, which was proven by the morphologies of synthesized materials shown in Figs. 1 and S2.

3.1.2. Morphology of materials

As shown in Fig. S2, the synthesized pure Ag_2S showed an irregular nanostructure (Fig. S2A & S2A1) while Ti_3C_2 displayed a smooth lamellar structure (Fig. S2B & S2B1). After a wet chemical reaction, numerous nanoparticles were uniformly distributed on the surface of the lamellar nanosheets (Fig. S2C and S2C1). The HRTEM images of Ag_2S and Ti_3C_2 further confirmed the irregular nanoparticles of synthesized Ag_2S (Fig. 1A) and the nanosheet-like structure of Ti_3C_2 (Fig. 1B). Fig. 1C clearly shows that Ag_2S nanoparticles were evenly distributed on Ti_3C_2 nanosheets. The point-scan energy dispersive spectroscopy (EDS) detection (Fig. 1E) of Fig. 1C shows that it contains elements such as Ti, C, Ag, and S. To get more accurate element content information, the surface scan EDS mapping by FE-SEM showed that the contents of C, S, Ag, and Ti in Ag_2S/Ti_3C_2-20 were 31.88 at.%, 12.71 at.%, 24.56 at.%, and 30.85 at.%, respectively (Fig. S3A & S3B). The HRTEM of Ag_2S/Ti_3C_2-20 showed the crystal domains of Ag_2S and Ti_3C_2 and their respective parallel lattice stripes (Fig. 1D). The d-spacing of 2.42 Å corresponds with the (013) crystal plane of Ag_2S, while the d-spacing of 2.15 Å corresponds with the (105) crystal plane of Ti_3C_2, which is in

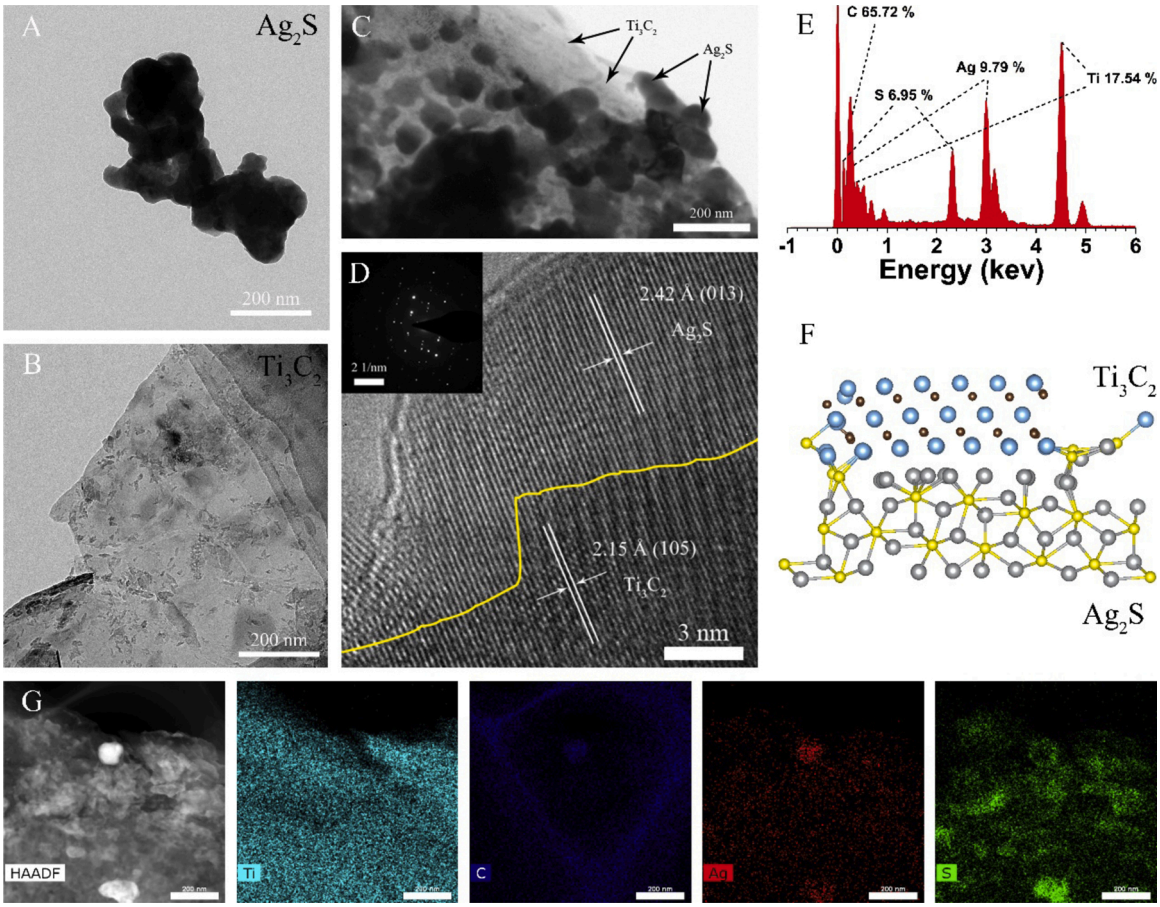

Fig. 1. TEM images of Ag_2S (A), Ti_3C_2 (B), and Ag_2S/Ti_3C_2-20 (C). (D) HRTEM image of Ag_2S/Ti_3C_2-20 with selected area electron diffraction patterns. (E) EDS detection of Ag_2S/Ti_3C_2-20 by TEM. (F) Structural model for theoretical calculations of Ag_2S/Ti_3C_2. (G) Elemental mapping of Ag_2S/Ti_3C_2-20 by TEM.

accordance with the inserted selected area electron diffraction (SAED) patterns [36]. This result indicated that Ag_2S and Ti_3C_2 were successfully compounded together tightly. Fig. 1F shows the front view of the atomic structure of the Ti_3C_2 layer and the (013) crystal plane of Ag_2S, which will be discussed in detail in the subsequent DFT calculations. The elemental mapping in the TEM image (Fig. 1G) clearly showed the uniform distribution of the elements of Ag, S, Ti, and C in Ag_2S/-Ti_3C_2-20, suggesting the uniform distribution of Ag_2S nanoparticles on Ti_3C_2 nanosheets, which is in agreement with Fig. S3C.

3.1.3. Material component characterization

The X-ray patterns of the synthesized samples are shown in Fig. 2A. The prepared Ag_2S showed obvious peaks of (111), (-112), (120), (-121), (-103), and (200) at 29.0°, 31.5°, 33.6°, 34.4°, 37.7°, and 43.4°, respectively, which corresponds to the characteristic peaks of Ag_2S [22, 35]. The XRD patterns (Fig. S4) of Ti_3C_2 before and after ultrasonic peeling with HF etching and intercalation showed crystalline surfaces at (002), (004), (105), and (110), corresponding to the characteristic peaks of Ti_3C_2 [36,37]. The characteristic peaks of both Ag_2S and Ti_3C_2 still appeared clearly on the X-ray diffractograms of the Ag_2S/Ti_3C_2 hybrid with a different mass ratio, with different intensity. The above results indicated the successful preparation of Ti_3C_2, Ag_2S, and Ag_2S/Ti_3C_2 hybrids. Fig. S5 shows the full spectrum of the Raman spectra of the synthesized materials in the range of 50–2000 cm^{-1}. Ag_2S showed no peaks. In contrast, strong Raman signals were detected from both Ag_2S/Ti_3C_2 hybrids and Ti_3C_2. The Raman signals of Ag_2S/Ti_3C_2-10, Ag_2S/Ti_3C_2-20, and Ag_2S/Ti_3C_2-40 gradually increased with the increase of Ti_3C_2 content in the hybrids. The enlarged Raman spectra in the range of 250–800 cm^{-1} showed obvious characteristic peaks of Ti_3C_2 at 414 cm^{-1} and 600 cm^{-1} (Fig. 2B), which is in accordance with previous results [38]. This result further indicates the successful preparation of Ag_2S/Ti_3C_2 hybrids. XPS examination was performed to investigate the functional groups and surface element valence states of Ti_3C_2 and Ag_2S in the hybrids. As shown in Fig. 2C, the survey scan of the Ag_2S/Ti_3C_2-40 shows the existence of the elements of Ag, S, Ti, and C in the hybrid. The narrow scan of Ag 3d displayed that two distinct peaks at 374.2 eV and 368.2 eV (Fig. 2D) are attributed to Ag $3d_{3/2}$ and Ag $3d_{5/2}$, respectively. In the case of S 2p, two peaks were located at 162.7 eV and 161.5 eV (Fig. 2E), which were assigned to S $2p_{1/2}$ and S $2p_{3/2}$, respectively. Together with XRD patterns, the above Ag 3d and S 2p signals should be obtained from the synthesized Ag_2S in hybrid [21]. As shown in Fig. 2F, Ti 2p is fitted into three peaks at 455.4 eV, 461.1 eV, and 456.4 eV, indicating that the main forms of Ti in the hybrid are Ti-C (Ti $2p_{3/2}$) and Ti (ii) [36,39,40]. The C 1s narrow scan (Fig. 2G) in the samples can be fitted into C-Ti, C—C, C—O, C═O, and O—C═O, respectively. The high resolution spectra of O 1s (Fig. 2H) can be fitted into two peaks at 531.2 eV and 532.9 eV, corresponding to Ti-OH and H_2O [40].

3.2. Density functional theory (DFT) theoretical calculations

3.2.1. Atomic structure simulation and density state analysis

DFT calculations were performed to study the structural properties and interface interactions between the two phases in the hybrid. During

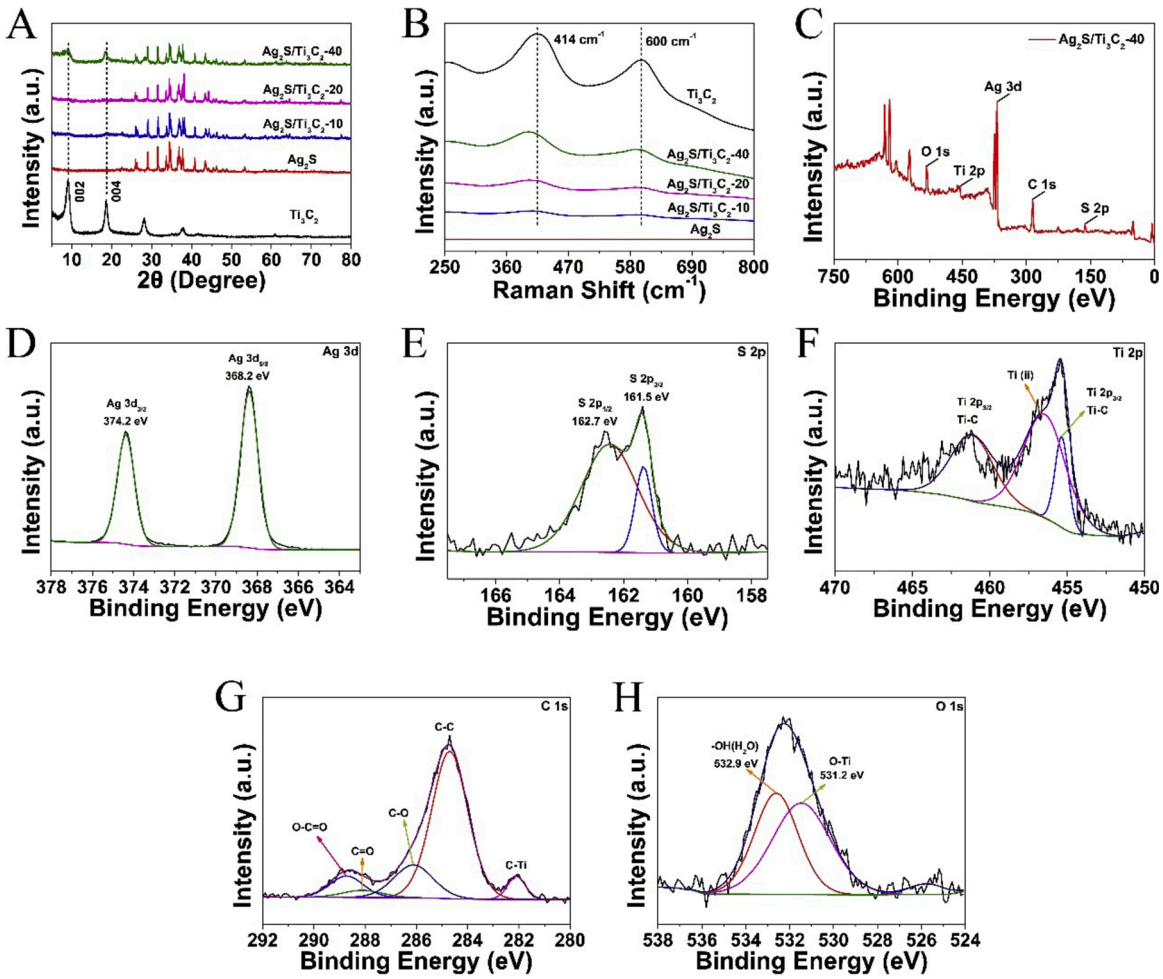

Fig. 2. XRD patterns (A) and Raman spectra (B) of Ti_3C_2, Ag_2S, Ag_2S/Ti_3C_2-10, Ag_2S/Ti_3C_2-20, and Ag_2S/Ti_3C_2-40. (C) The XPS survey spectrum of Ag_2S/Ti_3C_2-40. High-resolution XPS spectra of Ag 3d (D), S 2p (E), Ti 2p (F), C 1s (G), and O 1s (H) obtained from Ag_2S/Ti_3C_2-40.

DFT calculation, the atomic structures of the Ti_3C_2 layer and (013) crystal plane of Ag_2S were optimized. As shown in Fig. 3A, the side and top views of Ti_3C_2 show that Ti_3C_2 is a structurally regular laminar structure while Ag_2S is a slab model with a 013 plane. The side view of heterojunction displays that Ti_3C_2 and Ag_2S are tightly bound. To probe the heterojunction photocatalytic mechanism, the density of states (DOS) of Ag_2S, Ti_3C_2, and Ag_2S/Ti_3C_2 were calculated to investigate the degree of orbital contribution in the materials, respectively. The Fermi energy level (E_F) is set to 0 eV as a reference. The band gap size of Ag_2S is about 0.8 eV, as shown in the DOS results of Ag_2S (Fig. 3B), which is consistent with the subsequent experimental results. In addition, the valence band (VB) of Ag_2S consists mainly of d-p hybridization of Ag and S, while the conduction band (CB) of Ag_2S consists mainly of s-p hybridization of Ag and S. Fig. 3C shows that the VB of Ti_3C_2 consists mainly of the d-p hybridization of Ti and C, while the CB consists mainly of Ti-d. The CB and VB of Ti_3C_2 partially overlap each other, indicating the good electrical conductivity of Ti_3C_2. The DOS results of the heterojunction (Fig. 3D) showed that the VB of the Ag_2S (013)/Ti_3C_2 layer complex is mainly derived from the Ag-d of Ag_2S, while the CB is mainly derived from the Ti-d of Ti_3C_2. Moreover, the CB and VB of the heterojunction are partially overlapped together, suggesting that the conductivity of the hybrid is much better than that of Ag_2S. Therefore, the electrons of the Ag_2S/Ti_3C_2 heterojunction will jump from Ag-d of Ag_2S to Ti-d of Ti_3C_2 under 808 nm NIR light irradiation. These results indicate that during the photocatalytic process, the photogenerated electrons in Ag_2S are rapidly guided away by Ti_3C_2 and thus flow to the surface of Ti_3C_2, which extends the lifetime of the photogenerated electrons, thus improving the photocatalytic performance of the heterojunction [41].

3.2.2. *Electrostatic potential and built-in electric field simulation*

To further study the interface charge transfer path and formation mechanism of the Ag_2S/Ti_3C_2 heterojunctions, the electronic properties of Ti_3C_2, Ag_2S, and Ag_2S/Ti_3C_2 heterojunctions were evaluated by DFT calculation. As shown in Fig. 4A(A1) and B(B1), the calculated work function (WF) of the Ag_2S (013) plane and Ti_3C_2 layer is 4.45 eV and 4.00 eV, respectively, revealing the corresponding calculated Fermi levels of −1.12 eV and −1.45 eV *versus* vacuum level, respectively; *i.e.*, the Fermi level of Ti_3C_2 is lower than that of Ag_2S. Therefore, under dark conditions, when Ti_3C_2 and Ag_2S are in close contact, electrons on the surface of Ag_2S can flow into the surface of Ti_3C_2 through the interface. This result can be directly confirmed by the differences in plane average electron density (Fig. 4C) and the difference in three-dimensional charge density (Fig. 4C1), suggesting that there is a redistribution of charge at the interface of the Ag_2S/Ti_3C_2 heterojunction. In the constructed Ag_2S/Ti_3C_2 heterojunction model, the blue and yellow regions represent the electron depletion zone and the electron accumulation zone, respectively, and the difference in plane average electron density ($\Delta\rho$) also reveals the accumulation of electrons. The above calculation results show that once the Ag_2S nanoparticle contacts the Ti_3C_2 nanosheets tightly, a built-in electric field can be formed spontaneously at the interface between the two phases, inducing the formation of a Schottky heterojunction [42].

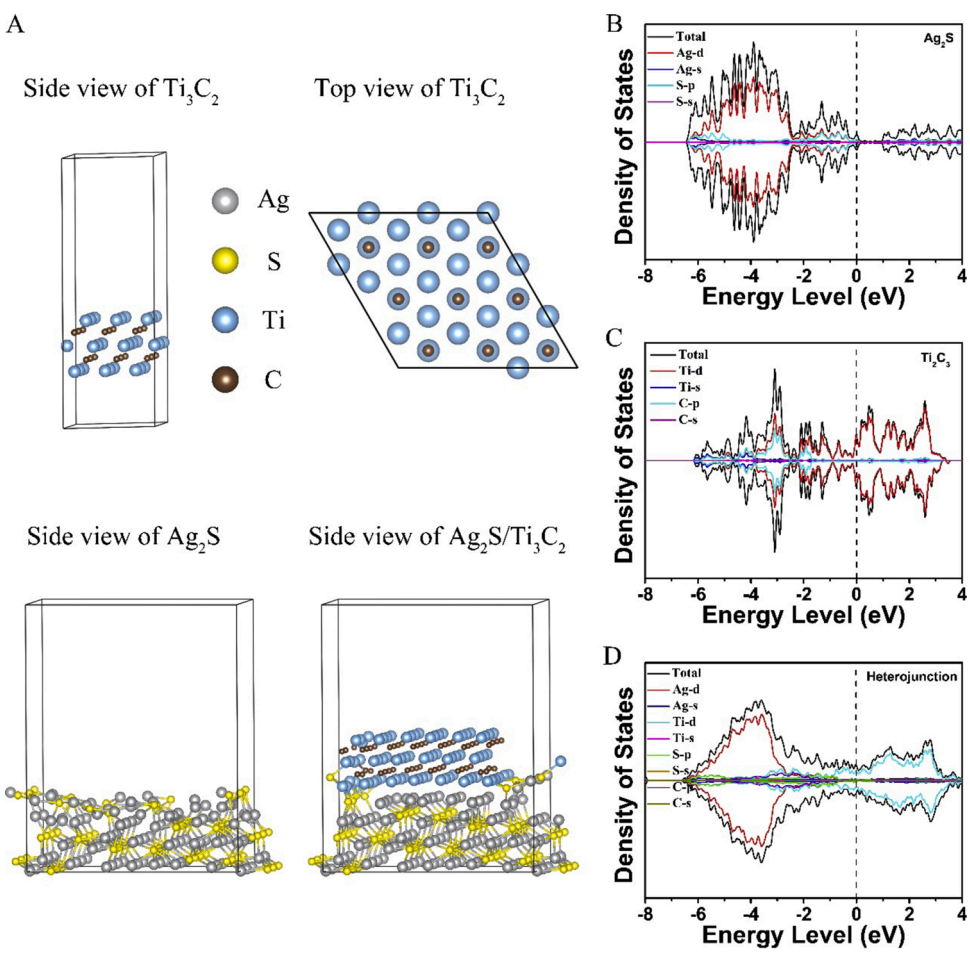

Fig. 3. (A) Structure model of Ti_3C_2, Ag_2S, and Ag_2S/Ti_3C_2 of different perspectives after structure optimization. Theoretical calculations of DOS of Ag_2S (B), Ti_3C_2 (C), and Ag_2S/Ti_3C_2 (D), respectively.

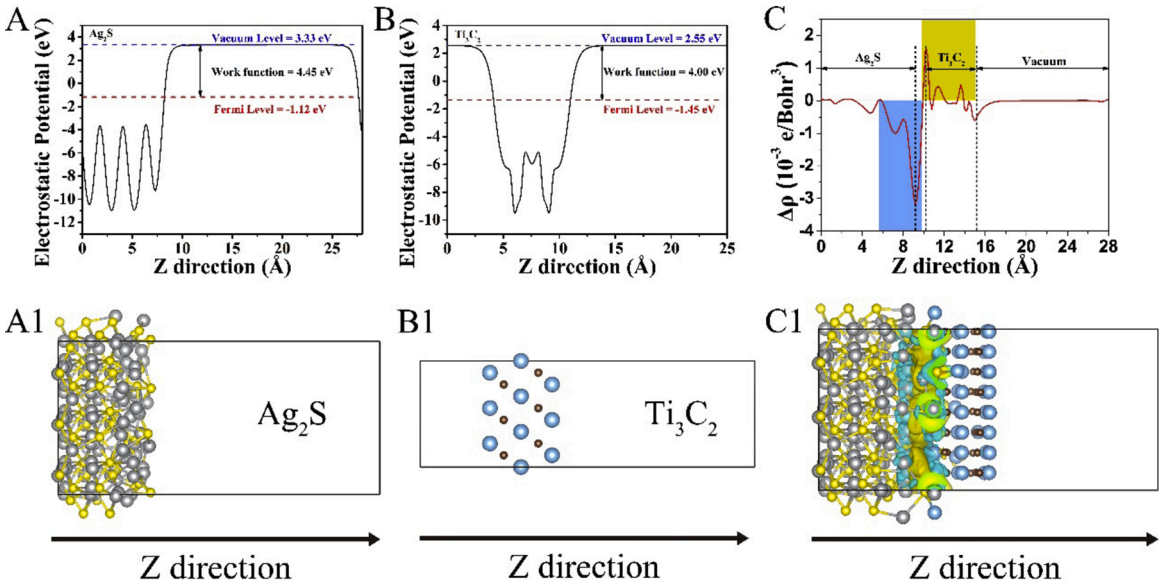

Fig. 4. (A) The calculated work function and (A1) corresponding structural model of (013) plane of Ag_2S. (B) The calculated work function and (B1) corresponding structural model of Ti_3C_2. (C) The difference in plane average electron density (Δρ) and the difference in three-dimensional charge density (C1) of Ag_2S/Ti_3C_2 heterojunction.

3.3. Photocatalytic performance evaluation

3.3.1. Band structure detection

Fig. S6A shows the UV–vis diffuse reflectance spectra of Ag_2S, Ti_3C_2, and Ag_2S/Ti_3C_2 hybrids. Since Ag_2S is a typical indirect semiconductor, the band gap energy relationship diagram of the sample (Fig. S6B-E) can be obtained by calculation based on the UV–vis spectra in Fig. S6A according to the Kubelka-Munk formula [17,43]. The calculated band gap of Ag_2S, Ag_2S/Ti_3C_2-10, Ag_2S/Ti_3C_2-20, and Ag_2S/Ti_3C_2-40 is 0.81, 0.77, 0.47, and 0.44 eV, respectively, suggesting the decreased band gap of the samples with the increase of Ti_3C_2 content in the hybrid, and thus resulting in the red-shift of absorption light. Therefore, increasing the content of Ti_3C_2 in the hybrid can increase the light absorption (Fig. S6F).

As shown in Fig. 5A, in the range of 360–1000 nm, the absorption intensity of pure Ti_3C_2 is the strongest, and pure Ag_2S shows the weakest absorption intensity. Meanwhile, the absorption intensities of Ag_2S/Ti_3C_2-10, Ag_2S/Ti_3C_2-20, and Ag_2S/Ti_3C_2-40 gradually increased, which is consistent with the above-mentioned results. That is to say, the introduction of Ti_3C_2 enhances the light-trapping ability of the hybrid heterojunction.

According to the ultraviolet photoelectron spectroscopy (UPS) spectra (Fig. 5B-D), the calculated work functions (Φ) of Ag_2S, Ti_3C_2, and Ag_2S/Ti_3C_2-20 are 3.9, 4.07, and 4.18 eV, respectively, based on the energy-level information derived from the UPS measurement (Fig. S7) and previous literature [44]. The energy difference between E_F and valence band (E_{VB}) comes from the low binding energy tail (E_{edge}) [45]. Thus, the E_{VB} and conduction band (E_{CB}) of Ag_2S are −4.47 eV and −3.66 eV, respectively. The E_{VB} and E_{CB} of the sample (Ag_2S/Ti_3C_2-20) after the combination of Ag_2S and Ti_3C_2 are −4.9 eV and −4.09 eV, respectively.

3.3.2. Photoelectrochemical detection

The photoelectrochemical properties of Ag_2S, Ti_3C_2, and Ag_2S/Ti_3C_2 hybrids were investigated and are shown in Fig. 5E. It is evident that the photocurrent intensity of the Ag_2S/Ti_3C_2 hybrids group is significantly higher than that of Ag_2S and Ti_3C_2, indicating that the combination of Ag_2S and Ti_3C_2 can effectively promote the separation of photogenerated electron-hole pairs and generate photogenerated charge carriers under NIR light irradiation. Among the Ag_2S/Ti_3C_2 hybrids, Ag_2S/Ti_3C_2-20 has the highest photocurrent intensity, followed by Ag_2S/Ti_3C_2-10 and Ag_2S/Ti_3C_2-40 has the relatively lowest. The electrochemical impedance spectroscopy (EIS) measurements (Fig. 5F) showed that the decreased slope of the curves as the Ti_3C_2 content in the heterojunction increased, suggesting that the increase of Ti_3C_2 content reduced the charge transfer resistance of the heterojunction and thus accelerated the charge transfer rate, which provided more charge carries for the following photocatalytic reactions. Since the recombination of photogenerated electron-holes will emit energy in the form of fluorescence, the higher photoluminescence (PL) intensity indicates the recombination of more photogenerated electron-hole pairs. Fig. 5G shows that higher Ti_3C_2 content in the heterojunction results in much lower PL intensity, indicating that the addition of Ti_3C_2 can be beneficial for separating photogenerated-electrons in the hybrid and thus enhancing the photocatalytic activity of the material. This result is in agreement with the above-measured photocurrent density.

3.3.3. Detection of reactive oxygen species produced by photocatalysis

As an ROS-sensitive sensor, 2,7-dichlorofluorescein diacetate (DCFH-DA) can sensitively detect the presence of ROS in the surrounding environment [46]. After being irradiated by 808 nm NIR light for 20 min, the results of the DCFH-DA assay (Fig. 5H) showed that the total ROS content in the Control (Ctrl), Ti_3C_2, Ag_2S, Ag_2S/Ti_3C_2-10, Ag_2S/Ti_3C_2-20, and Ag_2S/Ti_3C_2-40 groups changed by 4.06, 4.48, 35.87, 93.33, 101.33, and 92.59-fold, respectively. The Ti_3C_2 group showed a very low signal of almost the same as the control group, indicating no ROS production during the light exposure. Meanwhile, the Ag_2S group also exhibited little ROS yields during the light exposure. In contrast, all the hybrids showed much higher ROS yields, suggesting that the addition of Ti_3C_2 greatly enhances the photocatalytic performance of Ag_2S. Among the three hybrid groups, Ag_2S/Ti_3C_2-40 showed the lowest ROS yields with 20 min NIR light irradiation, which was attributed to the lowest content of Ag_2S in Ag_2S/Ti_3C_2-40. In addition, the ROS of the Ag_2S/Ti_3C_2-10 and Ag_2S/Ti_3C_2-20 groups showed the same trend within the first 4 min of light exposure, and the total amount of ROS generated by the Ag_2S/Ti_3C_2-20 group was slightly higher than that by the Ag_2S/Ti_3C_2-10 group in 20 min, suggesting that 20% (mass ratio of Ti_3C_2:Ag_2S) has the strongest photocatalytic performance under 808 nm NIR light excitation. The species of generated ROS were further determined by the photodegradation of 1,3-diphenylisobenzofuran (DPBF)

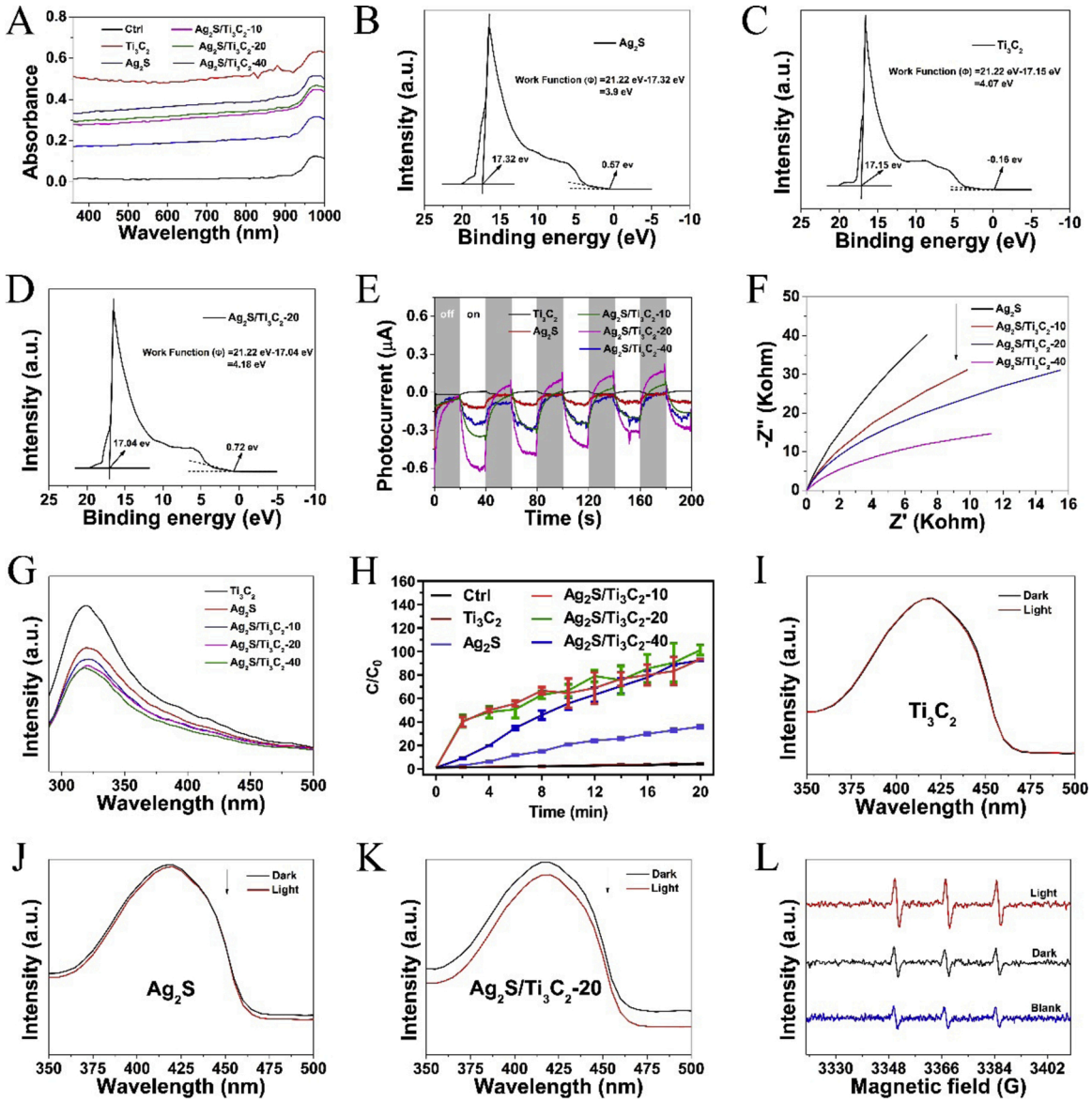

Fig. 5. (A) Absorption spectra of aqueous solutions of materials (500 μg/mL). UPS spectra of Ag_2S (B), Ti_3C_2 (C), and Ag_2S/Ti_3C_2-20 (D). Photoelectrochemical measurements including photocurrent responses (E) and EIS tests (F) of samples. (G) PL spectra of materials. (H) ROS production of samples detected by DCFH under 808 nm NIR irradiation. Detection of reactive oxygen species in photocatalytic processes: Degradation curves of DPBF of Ti_3C_2 (I), Ag_2S (J), and Ag_2S/Ti_3C_2-20 (K); (L) ESR measurements of Ag_2S/Ti_3C_2-20.

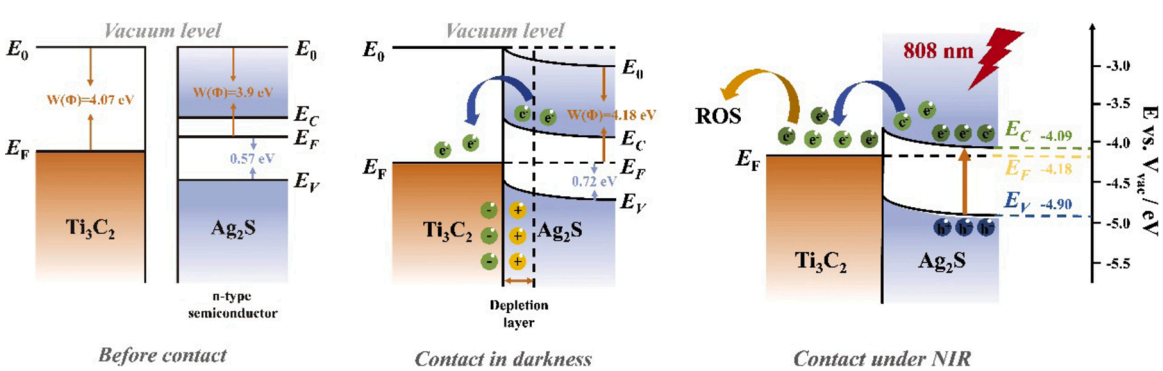

Fig. 6. Schematic diagram of the changes in the energy band structure and internal electric field near the interface of the two phases under different conditions (before contact, contact in darkness and contact under NIR) for Ti_3C_2 and Ag_2S, and the specific process of ROS production during photocatalysis.

and electron spin resonance (ESR) [47]. There was no decrease in the absorption peak around 415 nm in the Ti_3C_2 group before and after irradiation with 808 nm NIR light (Fig. 5I), while there was a slight decrease in the Ag_2S group (Fig. 5J). In contrast, a significant decrease was observed in the Ag_2S/Ti_3C_2-20 group (Fig. 5K). In addition, an ESR assay with 2,2,6,6-tetramethylpiperidine (TEMP) as a trapping agent showed the enhanced 1:1:1 signal in Ag_2S/Ti_3C_2-20 after light exposure (Fig. 5L). Both DPBF and ESR results showed that Ag_2S/Ti_3C_2-20 produced $^1O_2$ under 808 nm NIR light excitation. Overall, the above results indicate that Ag_2S/Ti_3C_2 hybrids have good photocatalytic activity under 808 nm NIR light irradiation, and the Ag_2S/Ti_3C_2-20 group has the strongest photocatalytic performance.

3.4. Photocatalytic mechanism of Ag_2S/Ti_3C_2

According to theoretical calculations and photocatalytic performance characterization results, the energy band structure diagram of Ti_3C_2 and Ag_2S in the photocatalytic process is shown in Fig. 6. Before Ti_3C_2 and Ag_2S contact, the calculated WF of Ti_3C_2 (4.07 eV) was greater than that of Ag_2S (3.9 eV) (Fig. 5B and C). After tightly contacting each other, the electrons tended to migrate from the side with a small WF to the surface of a material with a larger WF. Therefore, when Ag_2S contacted Ti_3C_2 under dark conditions, the electrons on the surface of the former flowed to the latter until the two Fermi levels reached a balance. In the equilibrium state, a Helmholtz electric double-layer structure was formed at the interface of Ti_3C_2 and Ag_2S. In the Helmholtz double-layer structure, Ti_3C_2 was negatively charged, and an electron-depletion layer formed near the surface of Ag_2S and was positively charged. Above theoretical calculations have confirmed that a built-in electric field is generated at the interface due to the redistribution of charges when the two phases are in contact (Fig. 4). According to the UPS calculation results, Ag_2S is a typical n-type semiconductor because its Fermi level is closer to CB. When the electrons in Ag_2S are repelled by the negatively charged Helmholtz layer in Ti_3C_2, the potential energy of the semiconductor rises, which eventually causes the energy band to bend upward [48].

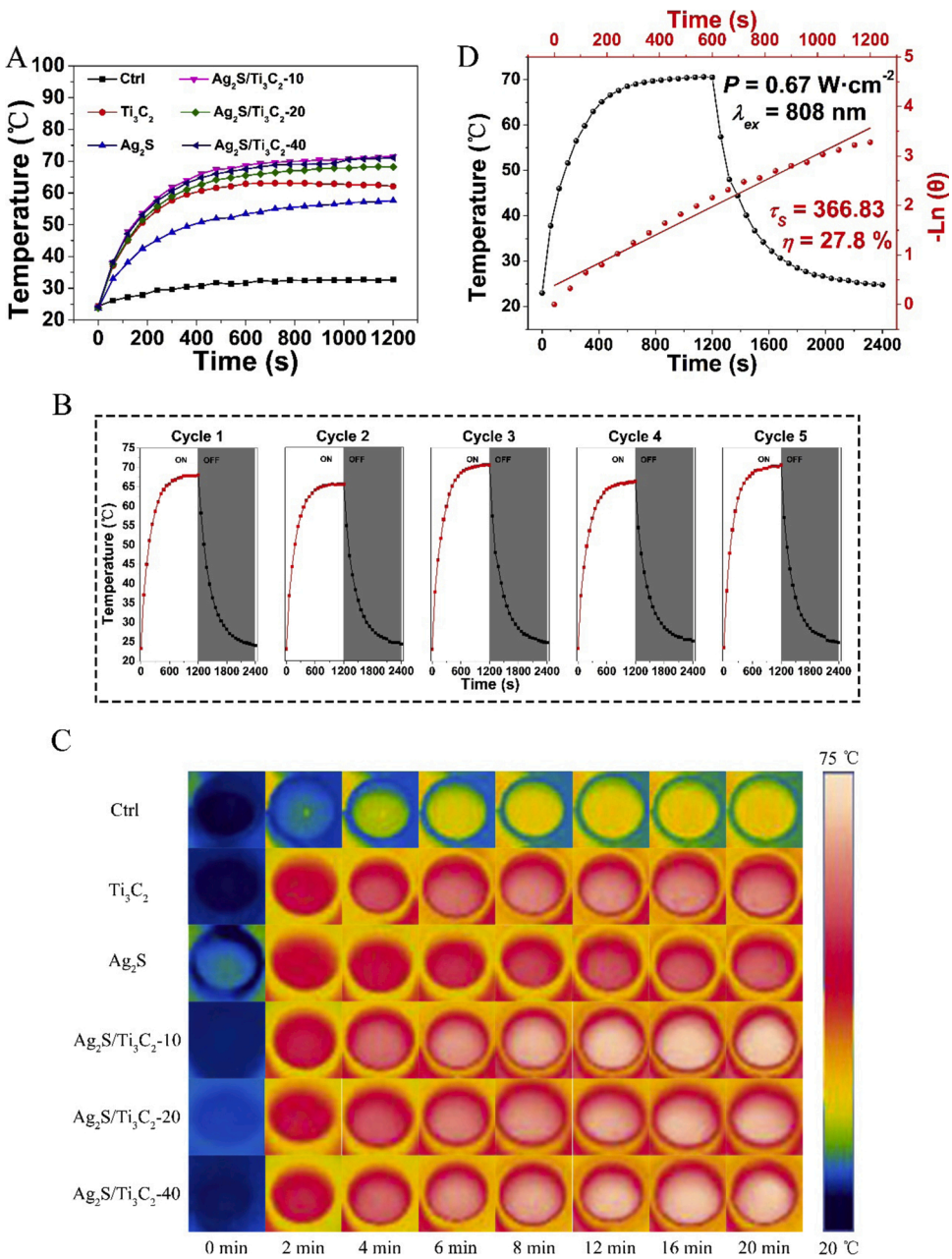

Fig. 7. The photothermal performance test of materials under 808 nm NIR (0.67 W/cm^2) irradiation conditions. (A) The photothermal heating curves of Ti_3C_2, Ag_2S, Ag_2S/Ti_3C_2-10, Ag_2S/Ti_3C_2-20, and Ag_2S/Ti_3C_2-40. (B) Photothermal cycle curves (5 cycles) of Ag_2S/Ti_3C_2-20. (C) Thermal images corresponding to the temperatures at different time points during the warming of the material in Fig. 7A. (D) Measurement and calculation of the photothermal conversion efficiency of Ag_2S/Ti_3C_2-20 under this irradiation condition.

Under 808 nm NIR light irradiation, Ag_2S was excited. Subsequently, the electron-hole pairs on the VB of Ag_2S separated, and the photogenerated electrons moved from VB to CB. Because of the bent-upward energy band of Ag_2S and its higher CB than E_F of Ti_3C_2, the photogenerated electrons on the CB of Ag_2S are more inclined to flow to the surface of Ti_3C_2 and be guided away rapidly, resulting in the effective separation of photogenerated electron-hole pairs. The separated photogenerated electrons and holes participate in the redox reaction in the environment to generate a large amount of ROS.

3.5. Photothermal performance

3.5.1. Exploration of photothermal performance

The photothermal properties of the materials were investigated under 808 nm NIR light irradiation by using the device diagram as shown in Fig. S10, where the concentration of the aqueous solution of the materials was kept the same as that used in the antibacterial experiments. Fig. 7A shows the photothermal temperature rise curve of the material. After 20 min of illumination, the temperature of the Ctrl, Ti_3C_2, and Ag_2S groups increased from room temperature (around 24.1 °C) to 32.7 °C, 62.1 °C, and 57.6 °C, respectively. The Ag_2S/Ti_3C_2-10, Ag_2S/Ti_3C_2-20, and Ag_2S/Ti_3C_2-40 groups increased from room temperature to 71.5 °C, 68.2 °C, and 71.1 °C, respectively. Fig. 7C shows the thermal images at different time points during the temperature rise of the material in Fig. 7A. The photothermal temperature rise curves and their corresponding thermograms can be used to visualize that the Ag_2S/Ti_3C_2 hybrids formed by the combination of Ag_2S and Ti_3C_2 have better photothermal conversion performance compared with those before the combination. We have measured five sets of photothermal ramp-up/down cycling curves for Ag_2S/Ti_3C_2-20, and the results show (Fig. 7B) that the heterojunction has good photothermal switching response performance and photothermal stability [49]. In addition, the photothermal conversion efficiency of Ag_2S/Ti_3C_2-20 (η = 27.8%) was calculated from the time constant (τ_S = 366.83) and the maximum steady-state temperature, as show in Fig. 7D [11]. This further demonstrates the ability of the heterojunction to convert 808 nm NIR light into thermal energy quickly and efficiently.

3.5.2. Photothermal mechanism

Under 808 nm NIR irradiation, the LSPR effect produced by Ti_3C_2 shows only lower photothermal performance [50]. The photogenerated hot electrons and holes of silver sulfide readily compound non-radiometrically in its deep defects to produce low-density phonons. The emitted phonons transfer the energy of the carriers to the lattice and generate heat by achieving lattice vibrations [51]. Based on the above discussion, the band gap of the composite decreases after the composite of Ag_2S and Ti_3C_2. As a result, the composites can generate more hot electrons under light excitation. These hot electrons not only heat up the lattice by generating a higher density of phonons in the deep defects of Ag_2S, but also transfer more to the Ti_3C_2 surface and generate more heat by enhancing the LSPR effect of Ti_3C_2. Therefore, the photothermal properties of the composites are effectively enhanced by the formation of heterojunctions between Ti_3C_2 and Ag_2S.

3.6. In vitro antibacterial activity assay

3.6.1. Antibacterial rate of materials

The antibacterial properties of the material solution (500 μg/mL) were tested against *S. aureus*. During the 808 nm laser irradiation for 20 min, due to the excellent photothermal effect of the material, we ensured that the temperature of the experimental group did not exceed 55 °C throughout to avoid the effect of excessive temperature on the antibacterial results and also to ensure safety (minimal invasion) and effective bacterial destruction [15]. Fig. 8A shows the antimicrobial plate-coating photos of the materials. The results (Fig. 8B) show that there is no significant difference in the number of colonies between Ctrl and material groups under dark conditions. This phenomenon clearly indicates that all samples did not have antimicrobial activity under dark conditions and reflects the good biocompatibility of the material itself. However, the antibacterial rates of Ti_3C_2, Ag_2S, Ag_2S/Ti_3C_2-10, Ag_2S/Ti_3C_2-20, and Ag_2S/Ti_3C_2-40 under light conditions were 76.71%, 62.48%, 97.54%, 99.99%, and 94.78%, respectively, as shown by the plate-coating photos and Fig. 8C. This result indicates that the photoexcited antibacterial performance of Ti_3C_2 and Ag_2S forming heterojunctions (Ag_2S/Ti_3C_2 hybrids) was greatly enhanced. Among the Ag_2S/Ti_3C_2 hybrids heterojunctions, the Ag_2S/Ti_3C_2-20 group had the most excellent and fastest bactericidal performance.

3.6.2. Antibacterial mechanism

To investigate the mechanism of the photoexcitation of materials for antimicrobial activity, we performed bacterial live-dead fluorescence staining and bacterial SEM tests on different samples under light and dark conditions, respectively. The green fluorescence in the live-dead fluorescence graph (Fig. 8D) was for live bacteria, while the red fluorescence was for dead bacteria. The results of the live-dead fluorescence staining showed that both the Ctrl and experimental groups fluoresced green under dark conditions, which indicated that the samples had no antibacterial ability under dark conditions. The fluorescence results of the Ctrl group under light conditions showed that *S. aureus* survived even under irradiation. However, the sample groups under light conditions showed different degrees of red fluorescence, with the Ti_3C_2 and Ag_2S groups showing smaller red fluorescence signals, while the Ag_2S/Ti_3C_2-10, Ag_2S/Ti_3C_2-20, and Ag_2S/Ti_3C_2-40 groups showed stronger red fluorescence signals. The bacterial live-dead fluorescence results remained consistent with the antibacterial results in Fig. 8A, B, and C. Again, this indicates that the antibacterial performance was greatly enhanced by the formation of heterojunctions (Ag_2S/Ti_3C_2 hybrids) between Ti_3C_2 and Ag_2S. Fig. 8E shows the FE-SEM images of *S. aureus*. The results show that the bacteria in the Ctrl and experimental groups were spherical and had smooth surfaces without defects under dark conditions, which indicates that the bacteria survived well in this condition. Under the light irradiation conditions, the surfaces of the bacteria in the experimental groups became rough and had different degrees of depression and breakage, except for the Ctrl group. This phenomenon indicated that the prepared Ag_2S/Ti_3C_2 hybrids effectively killed *S. aureus* under light irradiation. The Ag_2S/Ti_3C_2 hybrids were demonstrated to have good photothermal and photocatalytic properties. When the material was irradiated with 808 nm near-infrared light, the material PDT generated a large amount of ROS, while the excellent PTT of the material increased the ambient temperature of the bacteria. High temperatures caused irreversible bacterial destruction by denaturing the proteins of the bacteria. Also, high temperature levels increased the permeability of the bacterial membrane, which in turn allowed the $^1O_2$ produced during photocatalysis to proceed more easily into the bacteria. It caused the death of bacteria by damaging their cell membranes, proteins, and even DNA [52].

The wound healing tests showed that this hybrid system not only possessed highly effective antibacterial efficacy against *in vivo S. aureus* infection, but also had excellent biosafety, which were shown in Fig. S12-S15. The detailed experimental procedures, results and discussion of *in vivo* antibacterial tests and biosafety evaluation are shown in Supporting Information.

4. Conclusion

In summary, we have successfully prepared a novel 0D/2D Schottky heterojunction that has not been reported before by growing Ag_2S nanoparticles *in situ* on the surface of Ti_3C_2 using a simple wet chemical method. The structure optimization, DOS analysis, and charge-density calculation at the two-phase interface of the heterojunction were performed to elucidate in detail the electron transfer paths of the Ag_2S/Ti_3C_2 Schottky heterojunction in the photocatalytic process. The results

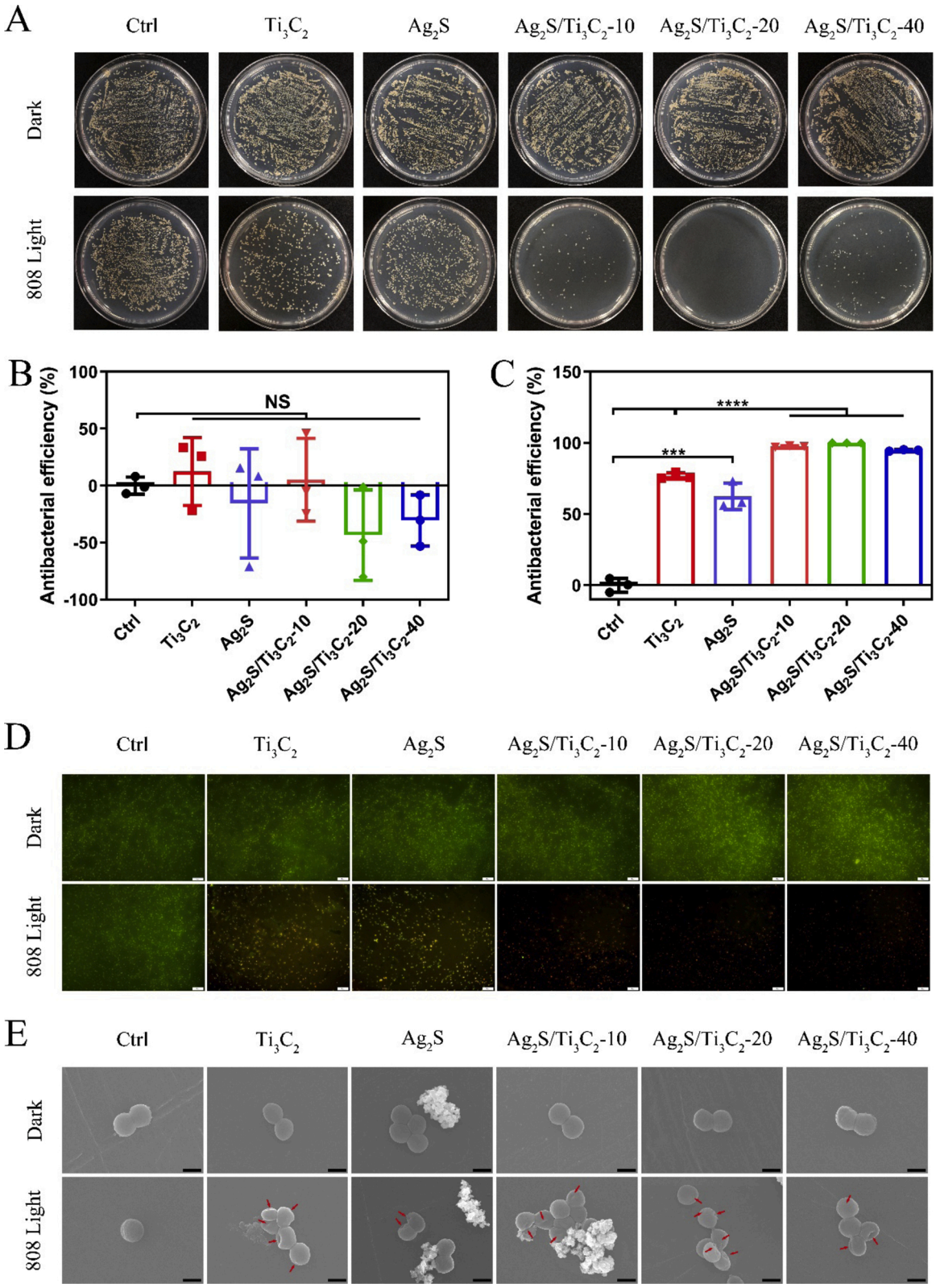

Fig. 8. *In vitro* antimicrobial performance and antimicrobial mechanism testing of materials. (A) Spread plate assay of *S. aureus* with samples after irradiation for 20 min of 808 nm NIR. Corresponding to the antibacterial rate counts under dark conditions (B) and 808 nm NIR irradiation conditions (C) in Fig. 8A. (D) Live-dead fluorescence images of *S. aureus*, live bacterium were stained green, and dead bacterium were stained red. Scale bar = 50 μm. (E) FE-SEM morphology of *S. aureus*, scale bar = 500 nm. Error bars indicate means ± standard deviations (n = 3): ***$P < 0.001$, ****$P < 0.0001$. NS, not significant ($P > 0.05$).

show that the introduction of Ti_3C_2 enhances the separation efficiency of the photogenerated charge carriers of the complexes and effectively transfers the photogenerated electrons. Therefore, the photocatalytic performance of Ag_2S/Ti_3C_2 Schottky heterojunctions and the ability to produce reactive oxygen species were enhanced. In addition, the heterojunction had an excellent photothermal effect, and the antimicrobial rate of PTT and PDT synergy of the heterojunction (Ag_2S/Ti_3C_2-20) was 99.99% under 808 nm NIR irradiation for 20 min. It also showed good therapeutic effects in *in vivo* antimicrobial tests. In addition, the material showed good biocompatibility *in vivo* and *in vitro*. These characteristics make this novel 0D/2D Schottky heterojunction promising as a highly efficient platform for the rapid treatment of bacterial infections with NIR. Most importantly, the present work provides a reliable way to explain the detailed mechanism in the heterojunction photocatalytic process and a scheme to optimize the photocatalytic activity of semiconductor photocatalysts.

CRediT authorship contribution statement

Qian Wu: Conceptualization, Methodology, Writing - original draft, Data curation, Investigation. **Lei Tan:** Methodology. **Xiangmei Liu:** Conceptualization, Writing - review & editing, Supervision, Project administration. **Zhaoyang Li:** Methodology. **Yu Zhang:** Conceptualization, Visualization, Writing - review & editing. **Yufeng Zheng:** Conceptualization, Writing - review & editing. **Yanqin Liang:** Methodology. **Zhenduo Cui:** Visualization. **Shengli Zhu:** Methodology. **Shuilin Wu:** Conceptualization, Writing - review & editing, Project administration.

Declaration of Competing Interest

The authors report no declarations of interest.

Acknowledgements

This work is jointly supported by the China National Funds for Distinguished Young Scientists (no. 51925104), the National Natural Science Foundation of China (no. 51871162 and 51801056), and Natural Science Fund of Hubei Province (no. 2018CFA064).

Appendix B. Supplementary data

Supplementary material related to this article can be found, in the online version, at doi:https://doi.org/10.1016/j.apcatb.2021.120500.

References

[1] M.S. Butler, A.D. Buss, Natural products—the future scaffolds for novel antibiotics? Biochem. Pharmacol. 71 (2006) 919–929.
[2] S.Y. Tong, J.S. Davis, E. Eichenberger, T.L. Holland, V.G. Fowler Jr., Staphylococcus aureus infections: epidemiology, pathophysiology, clinical manifestations, and management, Clin. Microbiol. Rev. 28 (2015) 603–661.
[3] Y. Qiao, X. Liu, B. Li, Y. Han, Y. Zheng, K.W.K. Yeung, C. Li, Z. Cui, Y. Liang, Z. Li, S. Zhu, X. Wang, S. Wu, Treatment of MRSA-infected osteomyelitis using bacterial capturing, magnetically targeted composites with microwave-assisted bacterial killing, Nat. Commun. 11 (2020), 4446.
[4] X. Lv, J. Zhang, D. Yang, J. Shao, W. Wang, Q. Zhang, X. Dong, Recent advances in pH-responsive nanomaterials for anti-infective therapy, J. Mater. Chem. B 8 (2020) 10700–10711.
[5] A.R. Brochado, A. Telzerow, J. Bobonis, M. Banzhaf, A. Mateus, J. Selkrig, E. Huth, S. Bassler, J. Zamarreno Beas, M. Zietek, N. Ng, S. Foerster, B. Ezraty, B. Py, F. Barras, M.M. Savitski, P. Bork, S. Gottig, A. Typas, Species-specific activity of antibacterial drug combinations, Nature 559 (2018) 259–263.
[6] M. Baym, L.K. Stone, R. Kishony, Multidrug evolutionary strategies to reverse antibiotic resistance, Science 351 (2016), aad3292.
[7] D.-G. Cai, M.-M. Bao, X.-Y. Wang, L. Yang, G.-W. Qin, R.-X. Wang, D.-F. Chen, E.-L. Zhang, Biocorrosion properties of Ti–$_3$Cu alloy in F ion-containing solution and acidic solution and biocompatibility, Rare Metals 38 (2019) 503–511.
[8] L. Li, H. Chang, N. Yong, M. Li, Y. Hou, W. Rao, Superior antibacterial activity of gallium based liquid metals due to Ga^{3+} induced intracellular ROS generation, J. Mater. Chem. B 9 (2021) 85–93.
[9] S. Yu, G. Li, P. Zhao, Q. Cheng, Q. He, D. Ma, W. Xue, NIR-laser-controlled hydrogen-releasing PdH nanohydride for synergistic hydrogen-photothermal antibacterial and wound-healing therapies, Adv. Funct. Mater. 29 (2019), 1905697.
[10] Y. Xu, X. Liu, Y. Zheng, C. Li, K.W.K. Yeung, Z. Cui, Y. Liang, Z. Li, S. Zhu, S. Wu, Ag_3PO_4 decorated black urchin-like defective TiO_2 for rapid and long-term bacteria-killing under visible light, Bioact. Mater. 6 (2021) 1575–1587.
[11] J. Li, X. Liu, Z. Zhou, L. Tan, X. Wang, Y. Zheng, Y. Han, D.-F. Chen, K.W.K. Yeung, Z. Cui, X. Yang, Y. Liang, Z. Li, S. Zhu, S. Wu, Lysozyme-assisted photothermal eradication of methicillin-resistant staphylococcus aureus infection and accelerated tissue repair with natural melanosome nanostructures, ACS Nano 13 (2019) 11153–11167.
[12] D. Han, Y. Han, J. Li, X. Liu, K.W.K. Yeung, Y. Zheng, Z. Cui, X. Yang, Y. Liang, Z. Li, S. Zhu, X. Yuan, X. Feng, C. Yang, S. Wu, Enhanced photocatalytic activity and photothermal effects of cu-doped metal-organic frameworks for rapid treatment of bacteria-infected wounds, Appl. Catal. B: Environ. 261 (2020), 118248.
[13] Y. Yang, P. He, Y. Wang, H. Bai, S. Wang, J.F. Xu, X. Zhang, Supramolecular radical anions triggered by bacteria in situ for selective photothermal therapy, Angew. Chem. Int. Ed. 56 (2017) 16239–16242.
[14] B. Ezraty, A. Gennaris, F. Barras, J.F. Collet, Oxidative stress, protein damage and repair in bacteria, Nat. Rev. Microbiol. 15 (2017) 385–396.
[15] J. Li, X. Liu, L. Tan, Z. Cui, X. Yang, Y. Liang, Z. Li, S. Zhu, Y. Zheng, K.W.K. Yeung, X. Wang, S. Wu, Zinc-doped prussian blue enhances photothermal clearance of staphylococcus aureus and promotes tissue repair in infected wounds, Nat. Commun. 10 (2019), 4490.
[16] L. Tan, J. Li, X. Liu, Z. Cui, X. Yang, S. Zhu, Z. Li, X. Yuan, Y. Zheng, K.W.K. Yeung, H. Pan, X. Wang, S. Wu, Rapid biofilm eradication on bone implants using red phosphorus and near-infrared light, Adv. Mater. 30 (2018), 1801808.
[17] Q. Wu, M. Zhou, Y. Gong, Q. Li, M. Yang, Q. Yang, Z. Zhang, Three-dimensional bandgap-tuned Ag_2S quantum dots/reduced graphene oxide composites with enhanced adsorption and photocatalysis under visible light, Catal. Sci. Technol. 8 (2018) 5225–5235.
[18] G.M. Neelgund, A. Oki, Photocatalytic activity of CdS and Ag_2S quantum dots deposited on poly(amidoamine) functionalized carbon nanotubes, Appl. Catal. B: Environ. 110 (2011) 99–107.
[19] B. Barrocas, T.J. Entradas, C.D. Nunes, O.C. Monteiro, Titanate nanofibers sensitized with ZnS and Ag_2S nanoparticles as novel photocatalysts for phenol removal, Appl. Catal. B: Environ. 218 (2017) 709–720.
[20] H. Yu, W. Liu, X. Wang, F. Wang, Promoting the interfacial H_2-evolution reaction of metallic Ag by Ag_2S cocatalyst: a case study of TiO_2/Ag-Ag_2S photocatalyst, Appl. Catal. B: Environ. 225 (2018) 415–423.
[21] M. Pang, J. Hu, H.C. Zeng, Synthesis, morphological control, and antibacterial properties of hollow/solid Ag_2S/Ag heterodimers, J. Am. Chem. Soc. 132 (2010) 10771–10785.
[22] K. Xiong, J. Li, L. Tan, Z. Cui, Z. Li, S. Wu, Y. Liang, S. Zhu, X. Liu, Ag_2S decorated nanocubes with enhanced near-infrared photothermal and photodynamic properties for rapid sterilization, Colloids Interface Sci. 33 (2019), 100201.
[23] C. Yang, Q. Tan, Q. Li, J. Zhou, J. Fan, B. Li, J. Sun, K. Lv, 2D/2D Ti_3C_2 MXene/g-C_3N_4 nanosheets heterojunction for high efficient CO_2 reduction photocatalyst: dual effects of urea, Appl. Catal. B: Environ. 268 (2020), 118738.
[24] T. Cai, L. Wang, Y. Liu, S. Zhang, W. Dong, H. Chen, X. Yi, J. Yuan, X. Xia, C. Liu, S. Luo, Ag_3PO_4/Ti_3C_2 MXene interface materials as a Schottky catalyst with enhanced photocatalytic activities and anti-photocorrosion performance, Appl. Catal. B: Environ. 239 (2018) 545–554.
[25] X. Han, L. An, Y. Hu, Y. Li, C. Hou, H. Wang, Q. Zhang, Ti_3C_2 MXene-derived carbon-doped TiO_2 coupled with g-C_3N_4 as the visible-light photocatalysts for photocatalytic H_2 generation, Appl. Catal. B: Environ. 265 (2020), 118539.
[26] H. Feng, W. Wang, M. Zhang, S. Zhu, Q. Wang, J. Liu, S. Chen, 2D titanium carbide-based nanocomposites for photocatalytic bacteriostatic applications, Appl. Catal. B: Environ. 266 (2020), 118609.
[27] S. Pan, J. Yin, L. Yu, C. Zhang, Y. Zhu, Y. Gao, Y. Chen, 2D MXene-integrated 3d-printing scaffolds for augmented osteosarcoma phototherapy and accelerated tissue reconstruction, Adv. Sci. 7 (2020), 1901511.
[28] X. Xie, N. Zhang, Positioning mxenes in the photocatalysis landscape: competitiveness, challenges, and future perspectives, Adv. Funct. Mater. 30 (2020), 2002528.
[29] J. Ran, G. Gao, F.T. Li, T.Y. Ma, A. Du, S.Z. Qiao, Ti_3C_2 MXene co-catalyst on metal sulfide photo-absorbers for enhanced visible-light photocatalytic hydrogen production, Nat. Commun. 8 (2017), 13907.
[30] G. Kresse, D. Joubert, From ultrasoft pseudopotentials to the projector augmented-wave method, Phys. Rev. B 59 (1999) 1758.
[31] J.P. Perdew, K. Burke, M. Ernzerhof, Generalized gradient approximation made simple, Phys. Rev. Lett. 77 (1996) 3865.
[32] H.J. Monkhorst, J.D. Pack, Special points for brillouin-zone integrations, Phys. Rev. B 13 (1976) 5188.
[33] J. Harl, L. Schimka, G. Kresse, Assessing the quality of the random phase approximation for lattice constants and atomization energies of solids, Phys. Rev. B 81 (2010), 115126.
[34] H. Lin, S. Gao, C. Dai, Y. Chen, J. Shi, A two-dimensional biodegradable niobium carbide (MXene) for photothermal tumor eradication in NIR-I and NIR-II biowindows, J. Am. Chem. Soc. 139 (2017) 16235–16247.
[35] Q. Lu, F. Gao, D. Zhao, Creation of a unique self-supported pattern of radially aligned semiconductor Ag_2S nanorods, Angew. Chem. Int. Ed. 41 (2002) 1932–1934.

[36] T.Y. Ma, J.L. Cao, M. Jaroniec, S.Z. Qiao, Interacting carbon nitride and titanium carbide nanosheets for high-performance oxygen evolution, Angew. Chem. Int. Ed. 128 (2016) 1150–1154.
[37] M. Ghidiu, M.R. Lukatskaya, M.Q. Zhao, Y. Gogotsi, M.W. Barsoum, Conductive two-dimensional titanium carbide' clay' with high volumetric capacitance, Nature 516 (2014) 78–81.
[38] S. Yang, J. Yao, H. Hu, Y. Zeng, X. Huang, T. Liu, L. Bu, K. Tian, Y. Lin, X. Li, S. Jiang, S. Zhou, W. Li, T. Bashir, J.-H. Choi, L. Gao, J. Zhao, Sonication-induced electrostatic assembly of an $FeCO_3$@Ti_3C_2 nanocomposite for robust lithium storage, J. Mater. Chem. A 8 (2020) 23498–23510.
[39] J. Ai, Y. Lei, S. Yang, C. Lai, Q. Xu, SnS nanoparticles anchored on Ti_3C_2 nanosheets matrix via electrostatic attraction method as novel anode for lithium ion batteries, Chem. Eng. J. 357 (2019) 150–158.
[40] L. Liu, Q. Zhao, R. Liu, L. Zhu, Hydrogen adsorption-induced catalytic enhancement over Cu nanoparticles immobilized by layered Ti_3C_2 MXene, Appl. Catal. B: Environ. 252 (2019) 198–204.
[41] J. Li, X. Liu, L. Tan, Y. Liang, Z. Cui, X. Yang, S. Zhu, Z. Li, Y. Zheng, K.W.K. Yeung, X. Wang, S. Wu, Light-activated rapid disinfection by accelerated charge transfer in red phosphorus/ZnO heterointerface, Small Methods 3 (2019), 1900048.
[42] P. Xia, S. Cao, B. Zhu, M. Liu, M. Shi, J. Yu, Y. Zhang, Designing a 0D/2D s-scheme heterojunction over polymeric carbon nitride for visible-light photocatalytic inactivation of bacteria, Angew. Chem. Int. Ed. 59 (2020) 5218–5225.
[43] A.I. Kryukov, A.L. Stroyuk, N.N. Zin'chuk, A.V. Korzhak, S.Y. Kuchmii, Optical and catalytic properties of Ag_2S nanoparticles, J. Mol. Catal. A Chem. 221 (2004) 209–221.
[44] W. Chen, Y. Wu, Y. Yue, J. Liu, W. Zhang, X. Yang, H. Chen, E. Bi, I. Ashraful, M. Gratzel, L. Han, Efficient and stable large-area perovskite solar cells with inorganic charge extraction layers, Science 350 (2015) 944–948.
[45] F. Liu, R. Shi, Z. Wang, Y. Weng, C.M. Che, Y. Chen, Direct z-scheme hetero-phase junction of black/red phosphorus for photocatalytic water splitting, Angew. Chem. Int. Ed. 58 (2019) 11791–11795.
[46] Y. Lin, D. Han, Y. Li, L. Tan, X. Liu, Z. Cui, X. Yang, Z. Li, Y. Liang, S. Zhu, S. Wu, Ag_2S@WS_2 heterostructure for rapid bacteria-killing using near-infrared light, ACS Sustain. Chem. Eng. 7 (2019) 14982–14990.
[47] Q. Zhang, X. Liu, L. Tan, Z. Cui, X. Yang, Z. Li, Y. Liang, S. Zhu, K.W.K. Yeung, X. Wang, Y. Zheng, S. Wu, A near infrared-activated photocatalyst based on elemental phosphorus by chemical vapor deposition, Appl. Catal. B: Environ. 258 (2019), 117980.
[48] Z. Zhang, J.T. Yates Jr., Band bending in semiconductors: chemical and physical consequences at surfaces and interfaces, Chem. Rev. 112 (2012) 5520–5551.
[49] Q. Wu, X. Liu, B. Li, L. Tan, Y. Han, Z. Li, Y. Liang, Z. Cui, S. Zhu, S. Wu, Y. Zheng, Eco-friendly and degradable red phosphorus nanoparticles for rapid microbial sterilization under visible light, J. Mater. Sci. Technol. 67 (2021) 70–79.
[50] J. Li, Z. Li, X. Liu, C. Li, Y. Zheng, K.W.K. Yeung, Z. Cui, Y. Liang, S. Zhu, W. Hu, Y. Qi, T. Zhang, X. Wang, S. Wu, Interfacial engineering of Bi_2S_3/$Ti_3C_2T_x$ MXene based on work function for rapid photo-excited bacteria-killing, Nat. Commun. 12 (2021), 1224.
[51] Y. Cheng, Y. Chang, Y. Feng, H. Jian, Z. Tang, H. Zhang, Deep-level defect enhanced photothermal performance of bismuth sulfide-gold heterojunction nanorods for photothermal therapy of cancer guided by computed tomography imaging, Angew. Chem. Int. Ed. 57 (2018) 246–251.
[52] C. Mao, Y. Xiang, X. Liu, Y. Zheng, K.W.K. Yeung, Z. Cui, X. Yang, Z. Li, Y. Liang, S. Zhu, S. Wu, Local photothermal/photodynamic synergistic therapy by disrupting bacterial membrane to accelerate reactive oxygen species permeation and protein leakage, ACS Appl. Mater. Interfaces 11 (2019) 17902–17914.